



HAL
open science

Residual stresses in thin walled-structures manufactured by directed energy deposition: In-situ measurements, fast thermo-mechanical simulation and buckling

Daniel Weisz-Patrault, Pierre Margerit, Andrei Constantinescu

► To cite this version:

Daniel Weisz-Patrault, Pierre Margerit, Andrei Constantinescu. Residual stresses in thin walled-structures manufactured by directed energy deposition: In-situ measurements, fast thermo-mechanical simulation and buckling. Additive Manufacturing, 2022, 56, pp.102903. 10.1016/j.addma.2022.102903 . hal-03873521v2

HAL Id: hal-03873521

<https://hal.science/hal-03873521v2>

Submitted on 28 Nov 2023

HAL is a multi-disciplinary open access archive for the deposit and dissemination of scientific research documents, whether they are published or not. The documents may come from teaching and research institutions in France or abroad, or from public or private research centers.

L'archive ouverte pluridisciplinaire **HAL**, est destinée au dépôt et à la diffusion de documents scientifiques de niveau recherche, publiés ou non, émanant des établissements d'enseignement et de recherche français ou étrangers, des laboratoires publics ou privés.



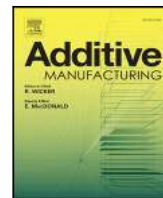
Distributed under a Creative Commons Attribution - NonCommercial - NoDerivatives 4.0 International License



Contents lists available at ScienceDirect

Additive Manufacturing

journal homepage: www.elsevier.com/locate/addma



Research Paper

Residual stresses in thin walled-structures manufactured by directed energy deposition: In-situ measurements, fast thermo-mechanical simulation and buckling

Daniel Weisz-Patrault^{a,*}, Pierre Margerit^b, Andrei Constantinescu^a

^a LMS, CNRS, École Polytechnique, Institut Polytechnique de Paris, F-91128 Palaiseau, France

^b PIMM, CNRS, Arts et Métiers, F-75013 Paris, France



ARTICLE INFO

Keywords:

Additive manufacturing
Direct Energy Deposition
Digital Image Correlation
In-situ experiments
Thermo-mechanical simulation

ABSTRACT

Manufacturing strains and subsequent residual stresses are key elements in the behavior of thin-walled structures, as they induce buckling, warping, and failure. This work proposes a combined experimental and numerical analysis of these features by investigating the additive manufacturing of a thin-walled structure using directed energy deposition.

In-situ measurements of temperature and in plan displacement fields during fabrication are identified over the entire part and all along the process by using infrared and optical cameras. One novelty of this work is to determine the displacement field without stopping fabrication unlike most of the existing approaches, which significantly simplifies the monitoring of the process.

In addition, a numerical modeling of the process has been developed to investigate the formation of residual stresses. One novelty of the proposed approach is to reach reasonably short computation time, by decoupling thermal and mechanical problems, which is interesting for parametric studies. Results are relevant, as the computed temperature and displacement fields are in good agreement with the in-situ measurements. A complementary buckling analysis also shows the ability of the model to predict when fabrication has to be stopped due to excessive out of plan deflection. The presented model can therefore be used as a tool to select suitable process parameters for a given part.

1. Introduction

The *Directed energy deposition* (DED) additive manufacturing (AM) technology has attracted significant interest in the recent years [1,2] as it enables to produce complex thin-walled structures with significant productivity. As in other AM technologies, the fabrication process involves the deposition of elementary metal volumes at temperatures significantly higher than the rest of the structure, which in turn is responsible for manufacturing strains and subsequently residual stresses. Residual stresses control is a major challenge in DED, as thin-walled structures are subjected to warping, buckling or fracture. Thus, prediction and control of residual stresses are key for the development of the technology and applications in mechanical engineering. Consequently, there has been a growing interest in monitoring the manufacturing process by installing in-situ measurement systems [3,4]. One of the objectives is to link the process parameters to the final microstructure and residual stresses (see for example [5–10]). However, there is a lack of fast predictive models of the process to consider extensive parametric studies to fine-tune the process parameters.

Residual stresses result from incompatible strains due to temperature gradients around the deposition zone, and are therefore a consequence of coupling between temperature kinetics and mechanical behavior. Ideally, in-situ observation should track simultaneously temperature and displacements fields or defects, and a series of results have been published in the last decade. A high-speed camera has been used to characterize laser–powder interaction in selective laser melting (SLM) additive manufacturing [11]. Moiré-like method has been utilized during fused deposition modeling process to retrieve distortions [12]. Surface topography has been measured by digital fringe projection techniques during SLM [13]. An In-situ multispectral photodetector has been used for porosity identification [14]. Adaptive vision-based detection of defects has been performed for DED in [15]. Residual stresses have been estimated applying a non-destructive post-processing using 3D digital image correlation (DIC) techniques in [16]. Unlike SLM, the part is easily observable during fabrication in DED, which facilitates the application of in-situ DIC techniques as reported

* Corresponding author.

E-mail address: daniel.weisz-patrault@cnrs.fr (D. Weisz-Patrault).

<https://doi.org/10.1016/j.addma.2022.102903>

Received 9 February 2022; Received in revised form 11 May 2022; Accepted 16 May 2022

Available online 23 May 2022

2214-8604/© 2022 Elsevier B.V. All rights reserved.

in [9,17]. However, these studies rely on painted speckle patterns that necessitate to interrupt fabrication, wait for the part to cool down completely before applying the paint and resume fabrication, which is very limiting for monitoring purposes. On the contrary, [18] used the natural contrast of the part to perform the DIC without paint. However, fabrication was interrupted to focus the camera.

In-situ experiments have also been developed for temperature measurements. Infrared thermography has been employed to study the influence of the melt pool temperature and cooling rates on microstructure evolution of 316L stainless steel [19,20], or to estimate temperature fields of thin-walled parts obtained by gas metal arc welding (GMAW) [21]. In addition, thermocouples fixed under the build platform, and infrared pyrometers have been used to validate simplified numerical simulations [22,23].

Despite of the coupling of the thermo-mechanical problem, only few studies have addressed simultaneous in-situ measurements of temperature and displacements. In [24], thermocouples, infrared imaging, displacement sensors and DIC techniques have been jointly employed to provide temperature and displacement fields in laser solid forming process. However, DIC is not performed on the part but only on the build platform using a painted speckle pattern.

The quantitative estimation of residual stresses necessitates not only a precise measurement of temperature and displacement fields but also a numerical simulation of the entire manufacturing process. One of the major difficulties stems from thermal and mechanical coupling at the origin of residual stresses, involving a wide range of time and space scales, ranging from the local scale of the fast moving high temperature melt pool with temperature gradients and cooling rates of the order of 10^6 to 10^7 K/m, and 10^4 to 10^5 K/s respectively, to the global scale of the manufacturing time of several hours and the centimeter-sized parts. On the one hand, many papers focus on very detailed simulations of the process, especially powder melting, the hydrodynamic problem determining the melt pool shape, and crystallization during cooling (see for example [25–32]). However, such numerical simulations are computationally costly and are often limited to a single layer. On the other hand, macroscopic simulations have been developed in order to simulate the entire process (see for example [6,9,17,24,33–39]). Nevertheless, these methods are computationally too costly to be applied to the modeling of complete structures, and are therefore inappropriate for parameter optimization.

As a consequence, there is a need for fast numerical simulations of the process for the computation of residual stresses during fabrication and after releasing of the build platform. Simplified linear thermal analyses have been proposed in [22,40], combining the image source method with the Rosenthal solution for a semi-infinite plate [41]. These methods are limited to simple flat-wall geometries and neglect heat sources due to solidification. Recently, a fast numerical approach has been proposed for the fully coupled thermo-metallurgical problem and applied for the manufacturing of thin-walled structures by DED [23, 42], which enables to consider complex geometry. This approach was used to predict grain growth during DED additive manufacturing [43] based on fast grain growth models [44,45].

The aim of this work is to conduct simultaneous infrared and visible light in-situ imaging of a thin-walled part during fabrication, and to provide a numerical strategy to estimate residual stresses. A first novelty is to perform the DIC on the entire part without stopping fabrication by only using the natural roughness of the part (i.e., without painted speckle pattern). Moreover, the DIC algorithm is applied backward in time. Thus, the reference configuration is the final part when all matter has been deposited and the final configuration is the deposition of the first layer, which enables to cover the complete deformation history of the complete part. A second novelty is the numerical strategy to compute the mechanical response and residual stresses, which is based on a weak coupling of thermal and mechanical problems and based on the temperature computation strategy developed by Weisz-Patrault [23]. Residual stresses during fabrication are then computed

Table 1
Chemical composition in weight percent.

Fe	Ni	Cr	Mo	Si	Mn	C	Others
Balance	12	17	2.5	2.3	1	0.03	≤0.5

by post-processing the thermal field within a finite element (FE) model, where the structure has been represented by shell elements. Thus, both the thermal and the FE model can rely on different time and space descriptions, which enables to significantly reduce computation time in comparison with a fully coupled thermo-mechanical model. Indeed, high cooling rates during solidification imply extremely fine time steps for the thermal problem, although structural mechanical effects take place at the scale of the entire structure, and do not necessitate such a fine time discretization. In addition, to capture mechanical structural effects, the entire geometry should be considered, although the thermal problem can be efficiently solved by exploiting specific simplifying assumptions, which enables to reduce the geometry dimension (e.g., heat fluxes are mostly aligned with the build direction, see. [23]). Therefore, the proposed model enables to reach short computation time, for instance only 20 min are necessary to simulate the construction of 30 layers of a 100 mm long thin-walled structure using a laptop with a 7-cores processor running at 2.7 GHz. Moreover predictions are in good agreement with experimental measurements. This opens up the perspective to answer parameter optimization problems.

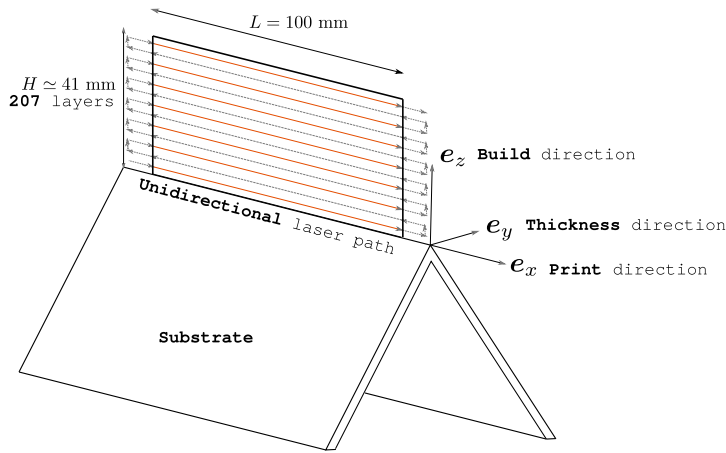
This paper is organized as follows. The experimental setup, emissivity calibration for the infrared camera, and the backward DIC procedure are detailed in Section 2. The following Section 3 presents the fast numerical simulation of the process, which enables to quantify residual stresses at all stages of the manufacturing process. The comparison between experiments and numerical results as well as general remarks are discussed in Section 4. In addition, a linear buckling analysis is provided to capture the interruption of fabrication due to excessive deflection, and a post-buckling analysis is provided to capture the final shape of the part. Conclusive remarks are provided in Section 5.

2. Experiments

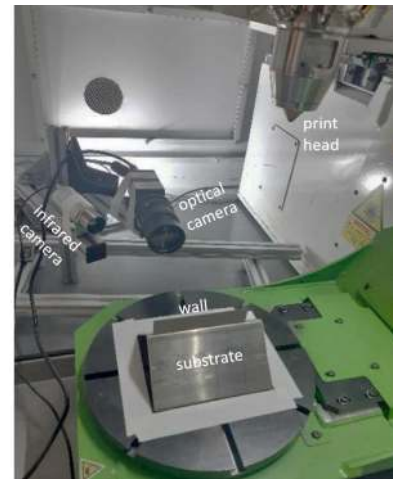
2.1. Fabrication

The material under scrutiny is a MetcoClad™ 316L-SI stainless steel, whose chemical composition is provided in Table 1. This grade is similar to AISI Type 316L (UNS S31603). However, MetcoClad™ has a higher content in silicon to prevent oxidation.

A thin-walled specimen has been additively manufactured with a DED technology, with a BeAM™ machine. The specimen length is $L = 100$ mm. The build platform, also denoted as the substrate, is a 2 mm thick plate made of 316L steel folded at 90° , as depicted in Fig. 1(a). The particular geometry of the substrate enables to avoid laser reflection on the substrate, which could disturb infrared measurements. The position of both infrared and optical cameras in the manufacturing enclosure is pictured in Fig. 1(b). In order to generate almost steady-state process parameters, the laser heat source is switched on during the forward displacement only, with a constant velocity $V_{\text{beam}} = 32.62$ mm/s and beam power $P_{\text{beam}} = 245$ W. As a consequence, a dwell time $t_{\text{dwell}} = 2.41$ s corresponding to the backward displacement is available between each layer, allowing to capture visible spectrum images without the presence of the intense laser light. The thin-walled structure is built with a constant layer height $h = 0.2$ mm up to buckling due to thermal and residual stresses. In the present case, the failure occurred after the fabrication of 207 layers, corresponding to an approximate wall height $H \approx 41$ mm.

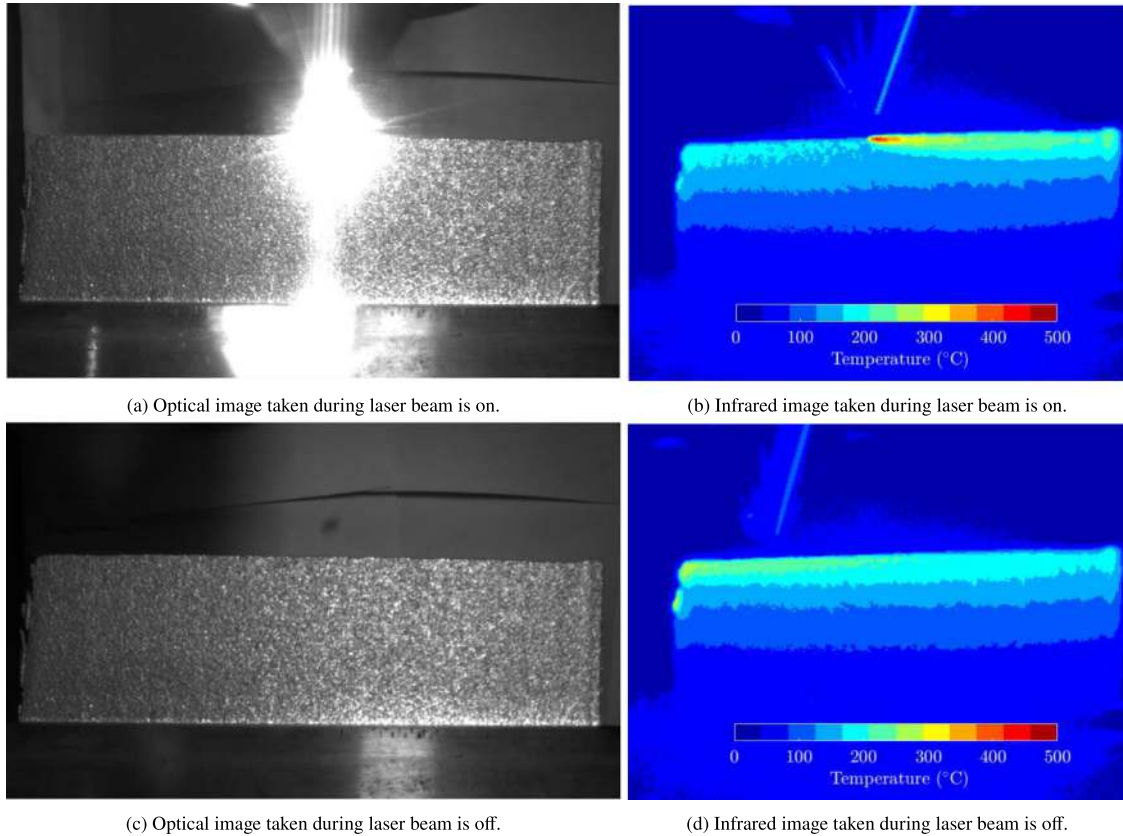


(a) Schematic view of fabrication.



(b) Picture of the experimental setup.

Fig. 1. Fabrication strategy and experimental setup.



(a) Optical image taken during laser beam is on.

(b) Infrared image taken during laser beam is on.

(c) Optical image taken during laser beam is off.

(d) Infrared image taken during laser beam is off.

Fig. 2. Comparison of images when the laser is on and off.

2.2. Temperature measurements

Thermal field measurements were conducted using an Optrix Xi 400™ infrared camera with a 288H × 382 W resolution. Thermocouple measurements on a similar printed structure heated by a hot plate allowed to finely calibrate the emissivity of the material. The obtained emissivity was approximately 0.32 on a temperature ranging from 20 to 500 °C. Two thermal images with the laser beam respectively switched on and off are displayed in Figs. 2(b) and 2(d). One can notice the moving heat source and the fast heat diffusion, which in turn enable to

neglect temperature gradients along the print direction in comparison with the build direction (see Weisz-Patrault [23]).

2.3. Distortion measurements

In plan displacements measurements are performed by backward DIC from a series of images acquired during fabrication. Optical images were captured using an Allied Vision Pike 505B™ camera with a 1506H × 2452 W resolution facing directly the wall with an additional lighting with a LED spotlight. To obtain the image contrast required for DIC analysis, the camera exposure parameters were carefully set

before fabrication on a test sample, which also prevents automatic exposure errors due to changing lighting situations. Two images with the laser beam respectively switched on and off are presented in Figs. 2(a) and 2(c). One can notice the disturbance created by the heat source in optical images. Therefore, only the images corresponding to the dwell state (i.e. when laser beam is switched off) may be used in the DIC.

In the current application, due to the layer-by-layer building process, the region of interest (ROI) in the DIC is continuously evolving, which implies a growing correlation domain $\Omega(t)$. The growth stops at the final stage at time t_f at which $\Omega(t_f)$ represents the entire manufactured part. In order to facilitate the analysis, the DIC procedure is not performed in chronological order, as the reference configuration would be different for each material point, since material points are added to the domain at a different times. Instead, the DIC procedure is performed *backward* in time, from the final stage to the initial stage, which enables to have a single reference configuration. A similar temporal backward DIC was employed in [46]. As a consequence the *reference* ROI $\Omega(t_f)$ is now well defined and contains all the material points. The position vectors in the *current* configuration $\Omega(t)$ and in the *reference* configuration $\Omega(t_f)$ are denoted respectively by $\mathbf{x}(t)$ and \mathbf{X} , and are associated to the *current* image g at time t and to the *reference* image G at time t_f . An image is defined here as an application associating to a position vector the value of the gray level of the corresponding pixel. The DIC procedure consists in finding a *backward transformation* map denoted by $\phi(\mathbf{X}, t) : \mathbf{X} \in \Omega(t_f) \mapsto \mathbf{x}(t) \in \Omega(t)$. The estimation of ϕ is an ill-posed problem that should be regularized using Tikhonov–Phillips method. The backward transformation ϕ is therefore the solution of the following optimization problem:

$$\phi = \min_{\phi^*} \left[\int_{\Omega(t_f)} [g(\phi^*(\mathbf{X}, t)) - G(\mathbf{X})]^2 d\Omega + \alpha_{\text{reg}} \int_{\Omega(t_f)} \|\nabla \mathbf{F}^*\|^2 d\Omega \right] \quad (1)$$

The first and second term in the preceding cost function represent the DIC and the regularizing function (where $\mathbf{F}^* = \nabla \phi^*$ is the transformation gradient), and α_{reg} is a regularization coefficient. The minimization problem (1) has been solved using an iterative Gauss–Newton algorithm. For further details about the DIC problem setting refer to [46, 47].

Consider a material point corresponding to the position vector \mathbf{X} in the reference configuration that is deposited at time t_0 in $\mathbf{x}_0 = \mathbf{x}(t_0)$. The displacement of this material point at time t reads $\mathbf{u}(\mathbf{X}, t) = \mathbf{x}(t) - \mathbf{x}(t_0)$, therefore:

$$\mathbf{u}(\mathbf{X}, t) = \phi(\mathbf{X}, t) - \phi(\mathbf{X}, t_0) \quad (2)$$

The minimization problem (1) along with (2) are used to compute the displacement field arising during fabrication.

3. Fast numerical simulation

This section presents the numerical strategy to compute residual stresses occurring during DED, which combines heat sources, heat conduction, solidification and mechanical deformation. However, one can split the problem into (i) a fully coupled thermo-metallurgical problem including solidification, solid-state phase transitions, and the underlying heat sources (i.e. enthalpy changes), and (ii) a subsequent mechanical problem relying on thermal information as input. This is justified as phase transitions induced by mechanical strains and self-heating can be neglected. It should be noted that a similar strategy has been successfully developed for a different process in [48].

As already mentioned, this strategy enables to use different numerical approaches and different time and space descriptions for each one of the two problems. Thus, the fully coupled thermo-metallurgical problem can be solved with the fast thermal analysis proposed by Weisz-Patrault [23], and then residual stresses are computed as a post-processing by using the free general purpose FE code *Cast3m* [49]. When the material undergoes solid-state phase transitions under stress, transformation induced plasticity arises [50]. However, solid-state

phase transitions are negligible, as austenitic 316L stainless steel has been used. Thus, transformation induced plasticity has not been considered, and thermal expansion is the only load for the mechanical problem.

For the sake of conciseness, the reader is referred to [23] for details regarding theoretical basis of the thermal analysis. In the following, the proposed mechanical model, which takes temperatures as input and provides residual stresses as output, is presented.

To save computation time, the part was meshed using shell elements (i.e., 2D Reissner–Mindlin theory) and the folded plate used as substrate was replaced by an equivalent beam elements (i.e., 1D Timoshenko theory). As shown in Fig. 3, there is an offset between the center of mass of the substrate section and the location of the interaction loads between the substrate and the part, which in turn results in bending. Thus, to correctly take into account the substrate behavior, a kinematic coupling between traction/compression and bending responses has been imposed to the beam. This kinematic coupling is modeled by relating the displacement of the beam along the print direction u_x and the section rotation θ as follows: $u_x = a \times \theta$ (where a denotes the offset). The equivalent section S_{sub} (mm²) and moment of inertia I_{sub} (mm⁴) are calibrated by fitting two elastic FE computations based respectively on shell and equivalent beam elements. As shown in Fig. 3, for this comparison the applied load is a uniform force per unit length changing sign at the center, and boundary conditions consist in blocking displacements (i.e., $u_x = 0$ along the print direction, and $u_z = 0$ along the build direction) at the location where the substrate is clamped. In addition, the substrate is assumed to remain purely elastic with temperature independent Young and shear moduli denoted by E_{sub} and μ_{sub} respectively.

The important step is adding new matter when the existing part has already undergone deformation. The bounding between new and existing matter is interpreted as a kinematic condition, which results in strain incompatibilities at the interface. Residual stresses are due to these strain incompatibilities irreversibly embedded in the part as well as the irreversible plastic strain generated in the melt pool vicinity due to significant thermal expansion. Thus, residual stresses are not released after complete cool down at a uniform temperature and detachment from the substrate.

The mechanical problem is solved incrementally, with time steps denoted by k corresponding to the growing domain Ω_k . At each time step, the initial stress, displacement and plastic strain fields read $\sigma_{k-1}(\mathbf{x})$, $\mathbf{u}_{k-1}(\mathbf{x})$, and $\epsilon_{k-1}^p(\mathbf{x})$ (for $\mathbf{x} \in \Omega_{k-1}$), and are obtained from the previous time step. The imposed thermal strain $\Delta \epsilon_k^{\text{th}}(\mathbf{x})$ at time step k reads:

$$\Delta \epsilon_k^{\text{th}}(\mathbf{x}) = \alpha (T_k(\mathbf{x}) - T_{k-1}(\mathbf{x})) \mathbf{I} \quad (3)$$

where α denotes the thermal expansion coefficient, and $T_k(\mathbf{x})$ is the temperature field at time step k , and \mathbf{I} is the second order identity tensor. Since fully liquid metal is deposited, the deposition temperature is higher than the liquidus temperature. Moreover, liquid material does not undergo significant stress in the melt pool, and therefore thermal expansion is only considered when solid-state has been reached, (i.e., temperature is below the solidus temperature).

In the following, an isotropic elasto-plastic material is considered with von Mises flow rule and kinematic hardening as thermal cycles are expected. Of course at high temperature visco-plasticity better describes the material behavior. However, since cooling rates are very significant, the time spent in visco-plastic regime is very short, and viscosity has been neglected. Since temperature significantly evolves during the process, mechanical material properties are updated from one time step to the other. Thus, the Young modulus $E(T)$, the shear coefficient $\mu(T)$, and the yield stress $\sigma_y(T)$ are given as functions of temperature. Linear laws are sufficient for the Young and shear moduli, which reads:

$$E(T) = E_0 (1 - \beta_E (T - T_0)) \quad (4)$$

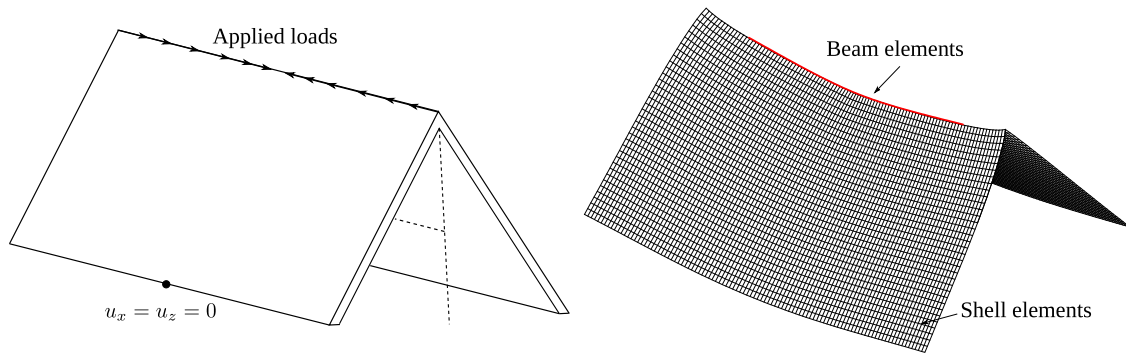


Fig. 3. Numerical simulation of the substrate to calibrate the equivalent beam.

where $T_0 = 273.15$ K, E_0 (MPa) is the Young modulus at T_0 , and β_E is a dimensionless coefficient.

$$\mu(T) = \mu_0 (1 - \beta_\mu (T - T_0)) \quad (5)$$

where μ_0 (MPa) is the shear modulus at T_0 , and β_μ is a dimensionless coefficient. An exponential law is however better suited for the yield stress, which reads:

$$\sigma_Y(T) = \sigma_0 [1 + \beta \exp(-\gamma(T - T_0))] \quad (6)$$

where σ_0 (MPa) is the yield stress at high temperature, $T_0 = 273.15$ K, and β, γ are dimensionless parameters. Hardening and thermal expansion coefficients respectively denoted by H_Y (MPa) and α (K⁻¹) are however considered as constant parameters.

It should be noted that material properties are usually subjected to statistical dispersion (e.g., variability of powder, fluctuations of process parameters etc.). Experimental investigations coupled with Bayesian calibration techniques could be used to determine a probability density function of material properties (see e.g., [51]). However, such a probabilistic framework has not been considered in this contribution as it would involve to perform several numerical simulations of the process for different draws of material parameters, which would significantly increase the computational cost.

As already mentioned, displacements along both the print and build directions are locked at the middle of the substrate beam denoted by \mathbf{x}_0 (i.e., $u_x(\mathbf{x}_0) = u_z(\mathbf{x}_0) = 0$). Free boundary conditions are imposed on the rest of the boundary (i.e., $\forall \mathbf{x} \in \partial\Omega_k / \{\mathbf{x}_0\}, \sigma_k(\mathbf{x}) \cdot \mathbf{n}(\mathbf{x}) = 0$, where \mathbf{n} is a unit normal vector). At each time step k the mechanical problem to solve reads:

$$\begin{cases} \operatorname{div}(\sigma_k) = 0 & \text{(equilibrium)} \\ \epsilon_k = \frac{1}{2} (\nabla \mathbf{u}_k + \nabla \mathbf{u}_k^T) & \text{(compatibility)} \\ \epsilon_k = \epsilon_k^e + \epsilon_k^p + \Delta \epsilon_k^{\text{th}} & \text{(strain decomposition)} \\ \sigma_k = 2\mu(T_k) \left(\epsilon_k^e + \frac{E(T_k) - 2\mu(T_k)}{2(3\mu(T_k) - E(T_k))} \operatorname{tr}(\epsilon_k^e) \mathbf{1} \right) & \text{(behavior)} \end{cases} \quad (7)$$

where ϵ_k^e denoted the elastic strain. The stress, displacement and plastic strain known from previous time step $k - 1$ are imposed as initial condition. The cumulative plastic strain rate reads $\dot{p}_{\text{cum}} = \sqrt{\frac{2}{3} \dot{\epsilon}_k^p : \dot{\epsilon}_k^p}$, and the elastic domain is defined by $f(\sigma_k) \leq 0$ where the function f reads:

$$f(\sigma_k) = \sqrt{\frac{3}{2} (s_k - \mathbf{X}_k) : (s_k - \mathbf{X}_k) - \sigma_Y(T_k)} \quad (8)$$

where s_k is the deviatoric stress, and \mathbf{X}_k is the center of the elastic domain. If $f(\sigma_k) < 0$ or if $f(\sigma_k) = 0$ and $(\partial f / \partial \sigma) : \dot{\sigma}_k < 0$, then the transformation is purely elastic (i.e., $\dot{\epsilon}_k^p = 0$). However, if $f(\sigma_k) = 0$ and $(\partial f / \partial \sigma) : \dot{\sigma}_k \geq 0$ plastic deformation takes place considering the

following flow rule and kinematic hardening:

$$\begin{cases} \dot{\epsilon}_k^p = \frac{3}{2} \left(\frac{s_k - \mathbf{X}_k}{\sigma_Y(T_k)} \right) \dot{p}_{\text{cum}} & \text{(flow rule)} \\ \dot{\mathbf{X}}_k = H_Y \dot{\epsilon}_k^p & \text{(kinematic hardening)} \end{cases} \quad (9)$$

In the following, the index k is discarded for the sake of clarity. For shell elements five generalized kinematic unknowns (degrees of freedom) are introduced: three translations denoted by u_x, u_y, u_z and two rotations denoted by φ_x, φ_z , where the print, thickness and build directions correspond to x, y, z respectively. Moreover the mechanical state relies on eight generalized stress components. Thus, the in-plane stress resultants \mathbf{N} , bending moments \mathbf{M} and shear resultants \mathbf{Q} are related to stresses as follows:

$$N_{ij} = \int_{-\frac{w}{2}}^{\frac{w}{2}} \sigma_{ij} dy \quad \left| \quad M_{ij} = \int_{-\frac{w}{2}}^{\frac{w}{2}} y \sigma_{ij} dy \quad \left| \quad Q_i = \int_{-\frac{w}{2}}^{\frac{w}{2}} \sigma_{iy} dy \quad (10)$$

where $(i, j) \in \{x, z\}^2$. From the computed quantities N_{ij}, M_{ij}, Q_i using the FE computation, one can compute an estimation of three dimensional Cauchy stresses, by assuming a linear dependence on the thickness direction y for σ_{ij} and homogeneous σ_{iy} (for $(i, j) \in \{x, z\}^2$) one obtains:

$$\begin{cases} \sigma_{ij} = \frac{12M_{ij}}{w^3} z + \frac{N_{ij}}{w} & \text{and } \sigma_{yy} = 0 \\ \sigma_{iy} = \frac{Q_i}{w} \end{cases} \quad (11)$$

where $(i, j) \in \{x, z\}^2$, and w denotes the layer thickness.

Within the framework of additive manufacturing, matter addition during the process has been traditionally modeled by one of the two FE techniques [28]: element *penalization* or element *activation*. Element penalization techniques consist in generating a single final mesh for the complete part and assign very low mechanical properties in all elements. Then, when new matter is progressively added to the part, realistic mechanical properties are assigned to the corresponding elements. The main drawback is that the stiffness matrix size corresponds to the entire part even at the beginning of fabrication. Element activation techniques consist in meshing at each time step only the actual part, which implies some sort of remeshing, which is the main drawback of the method. In *Cast3m* however, instead of remeshing the entire structure, a new sub-model containing the new element can be added to the existing model. But stiffness matrix assembling involves storing for each sub-model all the necessary information about the mechanical behavior. Thus, information about the mechanical behavior is repeated as many times as the number of elements in the structure, which tends to saturate the temporary memory (RAM), and to significantly slow down the computation.

In this contribution, a hybrid strategy between element penalization and element activation has been developed to overcome difficulties of both approaches. Instead of adding a new sub-model containing only one element to the existing model, a sub-model containing an

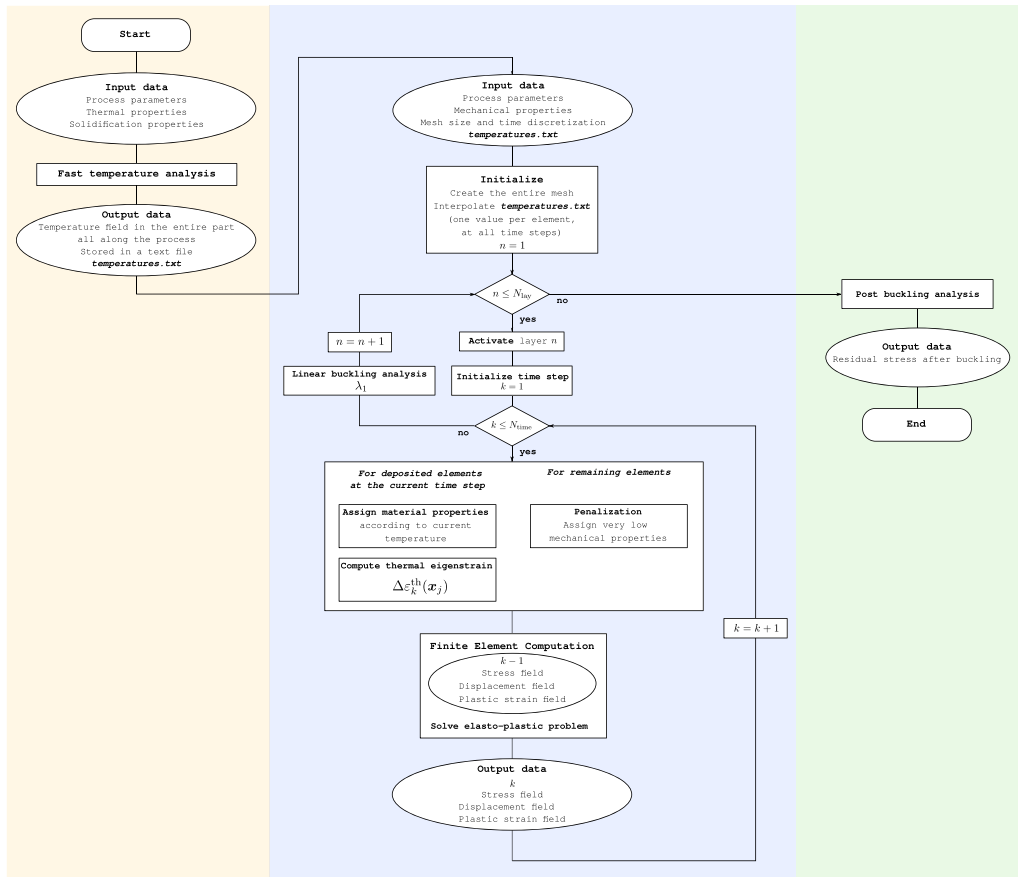


Fig. 4. Flowchart of the simulation framework (where N_{lay} denotes the number of layers, n the current layer, N_{time} the number of time steps per layer, and k the current time step).

entire layer is activated, which significantly reduces the number of sub-models (i.e., as many as the number of layers). In each layer, element penalization techniques are then used by progressively setting realistic material parameters in the elements (considering that the penalized Young modulus is set to 30 MPa). This hybrid approach enables us to benefit from element activation advantages without saturating the RAM.

A further memory saving feature is the fact that only one element is used along the layer height, because the aspect ratio of the elements should be kept in the order of 1 to avoid bad conditioning, which implies a rather thin mesh along the print direction.

In addition, to avoid exchanging large data files between the thermal model and the FE model, the temperature is extracted only at the center of each element at each time step. Therefore the imposed thermal strain (3) is defined as a constant piecewise field. High temperature gradients take place in the vicinity of the melt pool, and are smoothed by the proposed numerical implementation. However, since the mesh is rather thin along the print direction the loss of information associated to temperature gradients is reasonable. In addition, since the proposed approach is meant to study structural effects at the scale of the entire structure, this approximation is acceptable in this context. A flowchart of the simulation framework is provided in Fig. 4 to summarize the approach.

4. Results and discussion

4.1. Material parameters

A thin-walled structure has been additively manufactured with a unidirectional lasing strategy. Since the build platform is not a simple

horizontal plate with a known thickness as considered in [23], an equivalent thermal behavior has to be calibrated by adjusting the heat transfer coefficient (HTC) between the substrate and the air underneath denoted by \tilde{H}_{pla} , so that the substrate thermal behavior is sufficiently well captured. The deposition temperature denoted by T_{dep} is approximated as in [52] by the following analytical form:

$$T_{dep} = \frac{IR_{beam}}{\sqrt{\pi}\lambda_{liq}} \arctan\left(2\frac{\sqrt{D_{liq}t_{beam}}}{R_{beam}}\right) \quad (12)$$

Where R_{beam} is the laser beam radius, λ_{liq} and D_{liq} are respectively the thermal conductivity and diffusivity of the liquid metal, $I = P_{beam}/(2\pi R_{beam}^2)$ and $t_{beam} = R_{beam}/V_{beam}$ with V_{beam} the laser beam velocity.

Since we used the same machine and material as in [23], most parameters such as heat transfer coefficients, material properties or the extracted heat due to the gas flow carrying the powder, are identical. The reader is therefore referred to [23] for all the details. For the present thermal analysis, only the parameters specific to this study are listed in Table 2.

Temperature dependent material properties for the mechanical problem are fitted from data at high temperatures obtained in [53] for the yield stress and in [54] for Young and shear moduli, and at room temperature from data reported in previous studies [46,55] characterizing 316L obtained by the same DED process as used in the present work. However, data at high temperatures are provided for 316L obtained by other fabrication processes such as rolling. Since material properties depend on the microstructure resulting from the fabrication process, a bias may have been introduced, which is a limit of the proposed material properties identification. For instance the yield stress is presented as a function of temperature in Fig. 5. For temperatures higher than

Table 2
Material and simulation parameters for the thermal computation.

Number of layers	N_{lay}	(-)	250
Duration to build one layer	t_{lay}	(s)	3.10
Dwell time	t_{dwell}	(s)	2.41
Laser beam power	P_{beam}	(W)	245
Laser beam speed	V_{beam}	(mm/s)	32.62
Thermal conductivity of the liquid metal	λ_{liq}	(W mm ⁻¹ K ⁻¹)	0.035
Thermal diffusivity of the liquid metal	D_{liq}	(s ⁻¹ mm ²)	6.67
Laser beam radius	R_{beam}	(mm)	0.338
Build platform equivalent thickness	h_{pla}	(mm)	2
HTC build platform/air underneath	\tilde{H}_{pla}	(W m ⁻² K ⁻¹)	7000
Deposition temperature	T_{dep}	(K)	1858

Table 3
Material and simulation parameters for the mechanical computation. (Temperature dependence of material parameters is captured by simple laws whose coefficients are listed).

Equivalent beam for the substrate			
Section	S_{sub}	(mm ²)	32.5
Moment of inertia	I_{sub}	(mm ⁴)	30000
Offset	a	(mm)	35
Young modulus	E_{sub}	(MPa)	190000
Shear modulus	μ_{sub}	(MPa)	74218.75
Part			
Length of the thin-walled structure	L	(mm)	100
Layer thickness	w	(mm)	0.75
Layer height	h	(mm)	0.2
Mesh size (print direction)	Δ_x	(mm)	0.8
Mesh size (build direction)	Δ_z	(mm)	0.2
Young modulus at 273.15 K (4)	E_0	(MPa)	192835
Dimensionless coefficient (4)	β_E	(MPa/K)	4.2×10^{-4}
Shear modulus at 273.15 K (5)	μ_0	(MPa)	77765
Dimensionless coefficient (5)	β_μ	(MPa/K)	4.3×10^{-4}
Yield stress at high temperature (6)	σ_0	(MPa)	66
Dimensionless coefficient (6)	β	(-)	4.435
Dimensionless coefficient (6)	γ	(-)	2.236×10^{-3}
Hardening coefficient	H_Y	(MPa)	1200
Thermal expansion coefficient	α	(K ⁻¹)	19.2×10^{-6}

900 K, the yield stress $\sigma_Y(T)$ is extrapolated using the exponential law (6) in a range that has not been experimentally tested, which is also a limit of the proposed material properties identification. However, as shown in the following, computed displacements are in good agreement with DIC measurements, which confirms that the proposed approximate material properties are reasonable. The coefficients arising in (4), (5) and (6) are listed in Table 3, as well as simulation parameters and the identified properties of the equivalent beam for the substrate.

4.2. Comparison between in-situ measurements and numerical results

The proposed numerical strategy has been carried for 250 layers. The computation took approximately 24 h on a personal computer with a 7-cores processor running at 2.7 GHz, and only 20 min were needed to simulate 30 layers, which is an interesting result when compared to the 50 h reported in [9] for a similar 30 layers structure on a 6-cores workstation. Fabrication was stopped after 207 layers due to the buckling of the part and therefore following results are presented for the 207 layers structure.

A comparison between the temperature field obtained by the proposed numerical strategy and the infrared measurements is presented in Fig. 6. The infrared camera saturates at around 600 K, and the same scale has been used for the numerical simulation, even though temperatures reach much higher values near the melt pool. It should be noted that infrared pyrometers with higher temperature range have been used in [23] to validate the proposed thermal analysis. Good agreement between measurements and numerical results is observed in Fig. 6. In addition, thermal cycling is presented in Fig. 7 at four different positions along the build direction $z = 0$ mm, $z = 4.4$ mm,

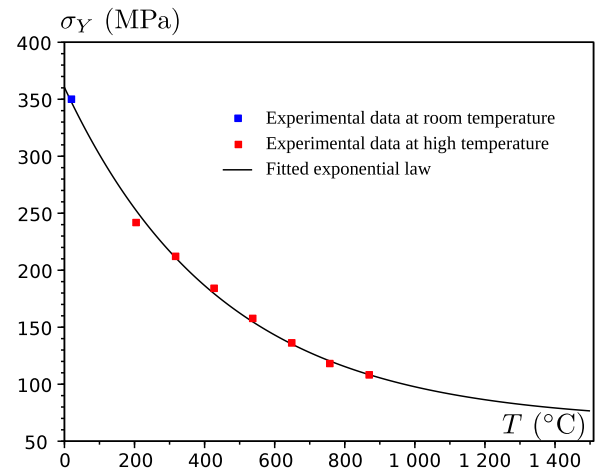


Fig. 5. Yield stress as a function of temperature. Experimental data at room temperature are extracted from [46,55] for 316L obtained by DED, and data at higher temperature are extracted from [53] for 316L obtained with different fabrication process.

$z = 10.8$ mm, and $z = 17.8$ mm. The numerical simulation is in good agreement with infrared measurements considering measurement uncertainties and modeling assumptions. More significant discrepancies are observed near the substrate, which may be explained by (i) difficulties in capturing the complex thermal behavior of the substrate, and (ii) difficulties to accurately measure the temperature near the substrate due to residual reflection.

Displacements along both print and build directions are compared to the DIC results in Fig. 8. Considering measurement uncertainties and resolution, very good global agreement is observed. Indeed, the correlation coefficient between computed and measured displacements is $r = 0.97$ for the print direction, and $r = 0.90$ for the build direction. However, measurements are slightly less symmetric than numerical results with respect to the central vertical axis of the wall, which is likely due to measurement uncertainties as significant regularization was necessary to perform the DIC procedure.

In addition, the identified components of the residual stress tensor (denoted by σ_{xx} , σ_{zz} , σ_{xz}) and the cumulative plastic strain (denoted by p_{cum}) are presented in Fig. 9 at the final stage of the build, when the part is fully cooled down and reached the room temperature. It should be noted that direct measurements of residual stresses (i.e., using X-ray diffraction techniques) have not been carried out to validate the estimated residual stress field because of significant surface roughness and unmelted particles. However, the material behavior is assumed to be sufficiently well known so that the good agreement between measured and computed displacements reported in Fig. 8 gives confidence in residual stresses presented in Fig. 9. High level of tension are observed along the print direction for the few last layers. Indeed, thermal contraction due to cooling in the last layers occur on a stiff body, which tends to generate tension. In addition, residual compression is significant along both the build and the print directions, which may result in buckling during the process. The cumulative plastic strain is significant and reaches at least 5%–7% in almost the entire part, and reaches 44%¹ near the substrate at the edges, which is due to the edge effect leading to very significant stress along the build direction.

4.3. Buckling analysis

As already mentioned, fabrication has been stopped at 207 layers because of the part buckling. In this section, a linear buckling analysis

¹ The scale has been saturated to 10% in Fig. 9 for the sake of readability.

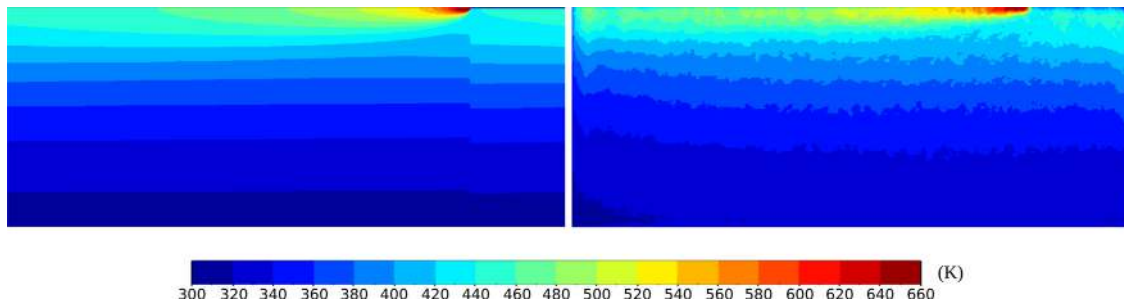


Fig. 6. Comparison of temperature fields between computation (left) and infrared camera measurements (right). The same colorbar is used for both figures. (For interpretation of the references to color in this figure legend, the reader is referred to the web version of this article.)

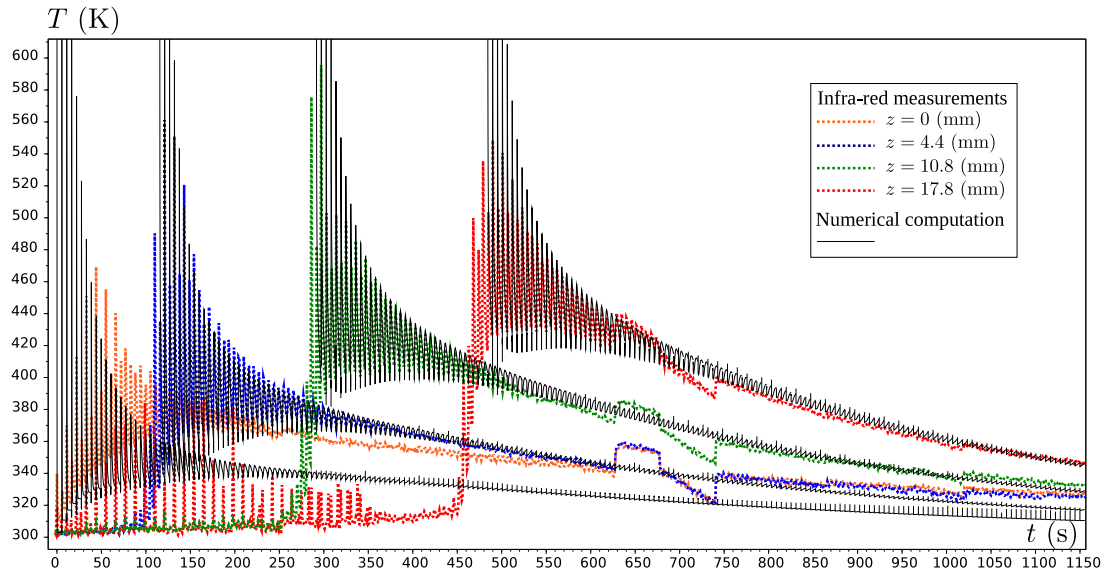


Fig. 7. Measured and computed temperature as a function of time for 4 positions along the build direction. Difficulties in thermal imaging have been noticed between 600 s and 750 s, which explains discrepancies in this time interval.

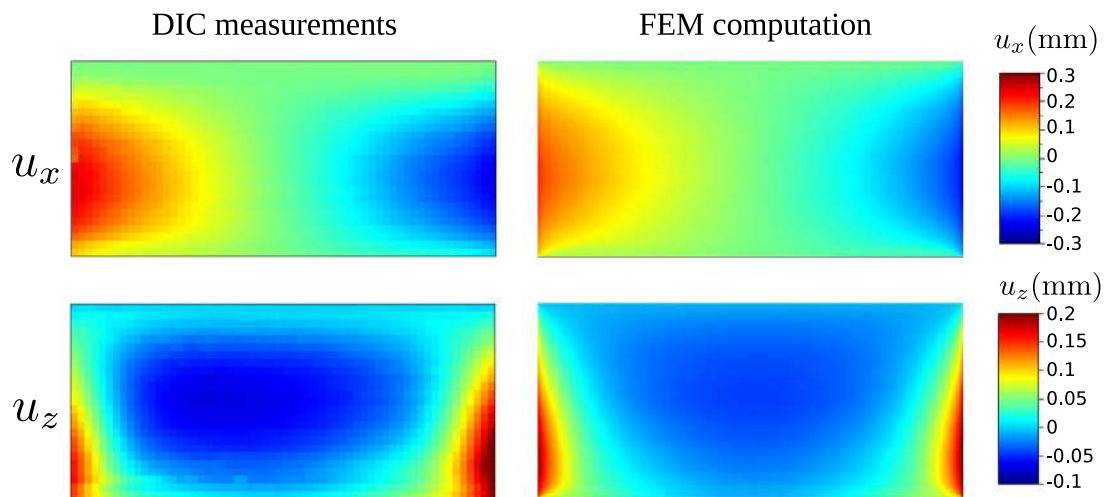


Fig. 8. Comparison of displacements along print and build direction for DIC measurements and FEM computation. The same colorbars are used for the DIC measurements and FEM computation. (For interpretation of the references to color in this figure legend, the reader is referred to the web version of this article.)

is proposed to determine whether the proposed approach enables us to capture, at least approximately, the risk of buckling resulting from the chosen process parameters. The linear buckling analysis is performed after the deposition of each layer. The residual stress field obtained in the proposed simulation is imposed, and the first mode critical factor

denoted by λ_1 (i.e., the amplification factor of the load needed to reach the critical load leading to buckling) is computed along with the corresponding deformation mode. The critical factor λ_1 is provided as a function of the layer number denoted by n in Fig. 10. For $n = 207$ the critical factor is $\lambda_1 \approx 1.4$, which is a reasonable buckling predictor,

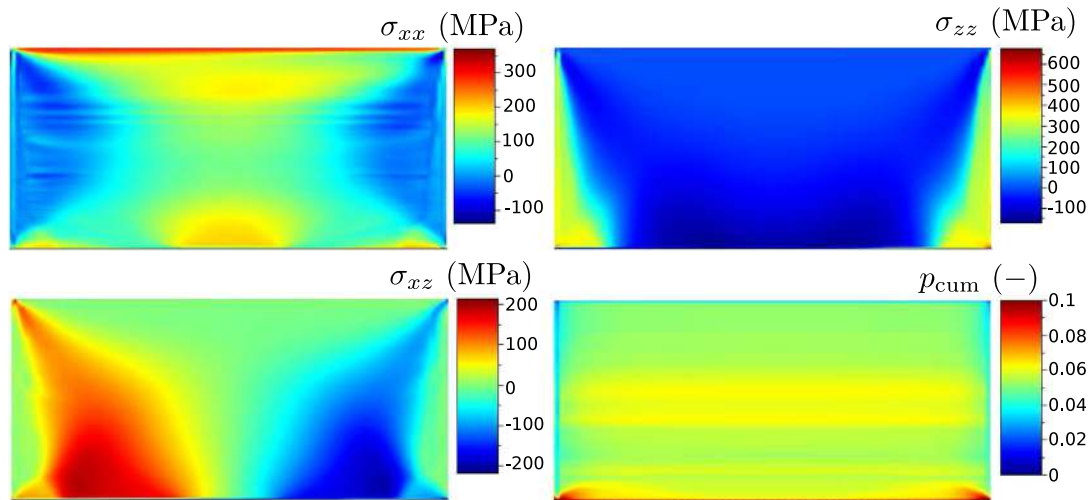


Fig. 9. Residual stress and cumulative plastic strain fields at the final stage, when the part is fully cooled down and reached the room temperature. (Oscillations may be noticed in the stress field along the print direction (i.e., σ_{xx}), which is likely due to the coarse mesh size.).

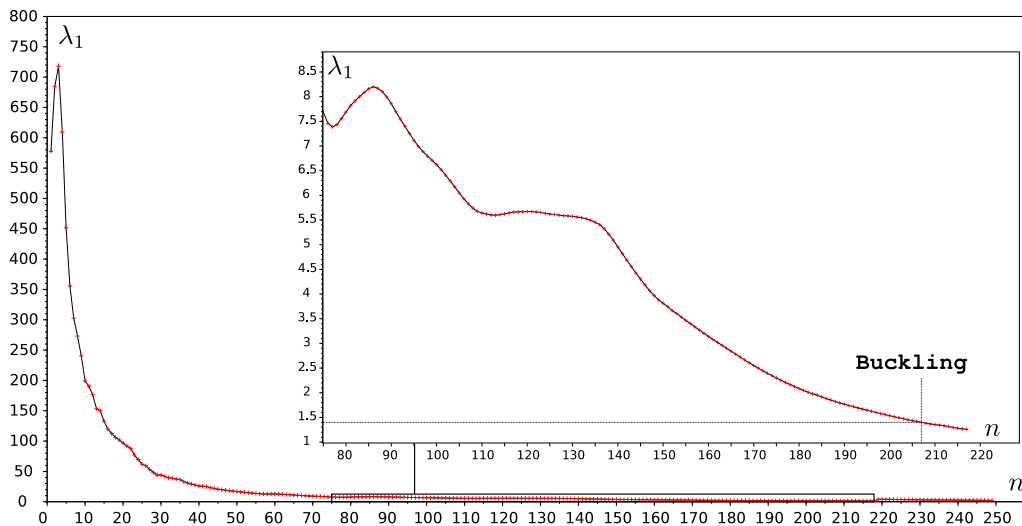


Fig. 10. Linear buckling analysis, λ_1 as a function of the layer number n .

as it is well known that critical factor overestimates the load for which buckling theoretically occurs for $\lambda_1 = 1$.

In addition, a post-buckling analysis has been conducted. The first mode of deflection has been computed (i.e., out of plan displacement field), and used to introduce a geometrical defect in the wall structure after 207 layers. The defect amplitude is set to half the wall thickness. Then, the stress field depicted in Fig. 9 is progressively applied under large displacement assumption (i.e., geometrical non-linearity). To avoid remeshing, the computation has been stopped for 95% of the load, as some mesh elements were undergoing excessive deformation, which would have needed to remesh. The corresponding out of plan deflection field is presented in Fig. 11, and reaches 1.2 mm, which is a sufficient misalignment between the part and the laser to make the fabrication fail. Thus, the proposed fast numerical strategy enables not only to estimate residual stresses arising during fabrication, but also to capture the resulting buckling behavior associated to specific process parameters.

5. Conclusion

In this paper, an in-situ experiment coupling both temperature and in plan displacement fields measurements is presented. Measurements

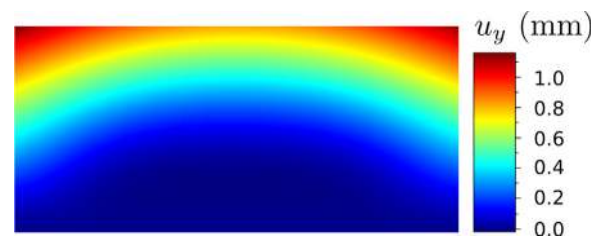


Fig. 11. First buckling mode of deflection.

have been carried out by infrared and optical cameras, without interrupting fabrication, and backward digital image correlation procedure has been used. The measurement system is easy to install and enables to monitor the most important quantities with respect to the formation of residual stresses (i.e., temperature and distortion).

In addition, a relatively fast numerical simulation of the process has been proposed. The model has been compared to the in plan displacement measurements, and good agreement has been observed (i.e., correlation coefficient $r \approx 0.97$ along the print direction and $r \approx 0.90$ along the build direction), which gives confidence in the estimation

of residual stresses. The cumulative plastic strain is around 5% in most of the part, and reaches 10 to 40% near the substrate. Compression reaches 100 MPa along both the print and the build directions. Thus, a linear buckling analysis has been provided to determine whether expected residual stresses result in buckling. Findings are consistent with the experiment as the computed first mode critical factor is around 1.4 when the fabrication has been stopped at 207 layers due to the part buckling. In addition, a post-buckling analysis also enables to capture the final shape (i.e., out of plan deflection), which is also in good agreement with the experiment (i.e., final shape of the part after buckling).

Thus, this work can be used as a tool to select suitable process parameters for a given part. Interesting outlooks stems from the coupling of fast numerical simulation and in-situ measurements for real time control of the process by using machine learning.

CRedit authorship contribution statement

Daniel Weisz-Patrault: Writing – original draft, Validation, Software, Methodology, Investigation, Data curation, Conceptualization. **Pierre Margerit:** Writing – original draft, Visualization, Validation, Investigation, Data curation, Conceptualization. **Andrei Constantinescu:** Writing – review & editing, Project administration, Funding acquisition, Conceptualization.

Declaration of competing interest

The authors declare that they have no known competing financial interests or personal relationships that could have appeared to influence the work reported in this paper.

Acknowledgment

This work has been financially supported by the Agence de l'innovation de défense, France.

References

- [1] W. He, W. Shi, J. Li, H. Xie, In-situ monitoring and deformation characterization by optical techniques; Part I: Laser-aided direct metal deposition for additive manufacturing, *Opt. Lasers Eng.* 122 (2019) 74–88.
- [2] Z. jue Tang, W. wei Liu, Y. wen Wang, K.M. Saleheen, Z. chao Liu, S. tong Peng, Z. Zhang, H. chao Zhang, A review on in situ monitoring technology for directed energy deposition of metals, *Int. J. Adv. Manuf. Technol.* 108 (11–12) (2020) 3437–3463.
- [3] S.K. Everton, M. Hirsch, P.I. Stavroulakis, R.K. Leach, A.T. Clare, Review of in-situ process monitoring and in-situ metrology for metal additive manufacturing, *Mater. Des.* 95 (2016) 431–445.
- [4] P. Charalampous, I. Kostavelis, D. Tzovaras, Non-destructive quality control methods in additive manufacturing: A survey, *Rapid Prototyp. J.* 26 (4) (2020) 777–790.
- [5] E.R. Denlinger, J.C. Heigel, P. Michaleris, T. Palmer, Effect of inter-layer dwell time on distortion and residual stress in additive manufacturing of titanium and nickel alloys, *J. Mater. Process. Technol.* 215 (2015) 123–131.
- [6] E.R. Denlinger, P. Michaleris, Effect of stress relaxation on distortion in additive manufacturing process modeling, *Addit. Manuf.* 12 (2016) 51–59.
- [7] Z. Wang, T.A. Palmer, A.M. Beese, Effect of processing parameters on microstructure and tensile properties of austenitic stainless steel 304L made by directed energy deposition additive manufacturing, *Acta Mater.* 110 (2016) 226–235.
- [8] B.A. Szost, S. Terzi, F. Martina, D. Boisselier, A. Prytuliak, T. Pirling, M. Hofmann, D.J. Jarvis, A comparative study of additive manufacturing techniques: Residual stress and microstructural analysis of CLAD and WAAM printed Ti–6Al–4V components, *Mater. Des.* 89 (2016) 559–567.
- [9] M. Biegler, B. Graf, M. Rethmeier, In-situ distortions in LMD additive manufacturing walls can be measured with digital image correlation and predicted using numerical simulations, *Addit. Manuf.* 20 (2018) 101–110.
- [10] X. Lu, X. Lin, M. Chiumenti, M. Cervera, Y. Hu, X. Ji, L. Ma, H. Yang, W. Huang, Residual stress and distortion of rectangular and S-shaped Ti-6Al-4V parts by directed energy deposition: Modelling and experimental calibration, *Addit. Manuf.* 26 (2019) 166–179.
- [11] U. Scipioni Bertoli, G. Guss, S. Wu, M.J. Matthews, J.M. Schoenung, In-situ characterization of laser-powder interaction and cooling rates through high-speed imaging of powder bed fusion additive manufacturing, *Mater. Des.* 135 (2017) 385–396.
- [12] J. Li, H. Xie, K. Ma, In-situ monitoring of the deformation during fused deposition modeling process using CGS method, *Polym. Test.* 76 (2019) 166–172.
- [13] B. Zhang, J. Ziegert, F. Farahi, A. Davies, In situ surface topography of laser powder bed fusion using fringe projection, *Addit. Manuf.* 12 (2016) 100–107.
- [14] M. Montazeri, A.R. Nassar, A.J. Dunbar, P. Rao, In-process monitoring of porosity in additive manufacturing using optical emission spectroscopy, *IISE Trans.* 52 (5) (2020) 500–515.
- [15] M.A. Naiel, D.S. Ertay, M. Vlasea, P. Fieguth, Adaptive vision-based detection of laser-material interaction for directed energy deposition, *Addit. Manuf.* 36 (2020) 101468.
- [16] J.L. Bartlett, B.P. Croom, J. Burdick, D. Henkel, X. Li, Revealing mechanisms of residual stress development in additive manufacturing via digital image correlation, *Addit. Manuf.* 22 (2018) 1–12.
- [17] M. Biegler, A. Marko, B. Graf, M. Rethmeier, Finite element analysis of in-situ distortion and bulging for an arbitrarily curved additive manufacturing directed energy deposition geometry, *Addit. Manuf.* 24 (2018) 264–272.
- [18] R. Xie, G. Chen, Y. Zhao, S. Zhang, W. Yan, X. Lin, Q. Shi, In-situ observation and numerical simulation on the transient strain and distortion prediction during additive manufacturing, *J. Manuf. Process.* 38 (2019) 494–501.
- [19] M.H. Farshidianfar, A. Khajepour, A. Gerlich, Real-time control of microstructure in laser additive manufacturing, *Int. J. Adv. Manuf. Technol.* 82 (5–8) (2016) 1173–1186.
- [20] M.H. Farshidianfar, A. Khajepour, A.P. Gerlich, Effect of real-time cooling rate on microstructure in laser additive manufacturing, *J. Mater. Process. Technol.* 231 (2016) 468–478.
- [21] D. Yang, G. Wang, G. Zhang, Thermal analysis for single-pass multi-layer GMAW based additive manufacturing using infrared thermography, *J. Mater. Process. Technol.* 244 (2017) 215–224.
- [22] C. Guévenoux, M. Nasiry, S. Durbecq, A. Charles, E. Charkaluk, A. Constantinescu, Thermal modeling of DED repair process for slender panels by a 2D semi-analytic approach, 2020.
- [23] D. Weisz-Patrault, Fast simulation of temperature and phase transitions in directed energy deposition additive manufacturing, *Addit. Manuf.* 31 (2020) 100990.
- [24] X. Lu, X. Lin, M. Chiumenti, M. Cervera, Y. Hu, X. Ji, L. Ma, W. Huang, In situ measurements and thermo-mechanical simulation of Ti–6Al–4V laser solid forming processes, *Int. J. Mech. Sci.* 153–154 (2019) 119–130.
- [25] D. Carron, P. Le Masson, R. Fabbro, 2D longitudinal modeling of heat transfer and fluid flow during multilayered direct laser metal deposition process, *J. Laser Appl.* 24 (3) (2012).
- [26] A. Yadollahi, N. Shamsaei, S.M. Thompson, D.W. Seely, Effects of process time interval and heat treatment on the mechanical and microstructural properties of direct laser deposited 316L stainless steel, *Mater. Sci. Eng. A* 644 (2015) 171–183.
- [27] V. Manvatkar, A. De, T. DebRoy, Spatial variation of melt pool geometry, peak temperature and solidification parameters during laser assisted additive manufacturing process, *Mater. Sci. Technol.* 31 (8) (2015) 924–930.
- [28] M. Megahed, H.-W. Mindt, N. N'Dri, H. Duan, O. Desmaison, Metal additive-manufacturing process and residual stress modeling, *Integr. Mater. Manuf. Innov.* 5 (1) (2016) 61–93.
- [29] E. Kundakcioglu, I. Lazoglu, S. Rawal, Transient thermal modeling of laser-based additive manufacturing for 3D freeform structures, *Int. J. Adv. Manuf. Technol.* 85 (1–4) (2016) 493–501.
- [30] Y. Lian, S. Lin, W. Yan, W.K. Liu, G.J. Wagner, A parallelized three-dimensional cellular automaton model for grain growth during additive manufacturing, *Comput. Mech.* 61 (5) (2018) 543–558.
- [31] H. Wei, G. Knapp, T. Mukherjee, T. DebRoy, Three-dimensional grain growth during multi-layer printing of a nickel-based alloy inconel 718, *Addit. Manuf.* 25 (2019) 448–459.
- [32] C. Kumara, A. Segerstark, F. Hanning, N. Dixit, S. Joshi, J. Moverare, P. Nylén, Microstructure modelling of laser metal powder directed energy deposition of alloy 718, *Addit. Manuf.* 25 (2019) 357–364.
- [33] M. Chiumenti, M. Cervera, A. Salmi, C.A. De Saracibar, N. Dialami, K. Matsui, Finite element modeling of multi-pass welding and shaped metal deposition processes, *Comput. Methods Appl. Mech. Engrg.* 199 (37–40) (2010) 2343–2359.
- [34] G. Marion, G. Cailletaud, C. Colin, M. Mazière, A finite element model for the simulation of direct metal deposition, in: *International Congress on Applications of Lasers & Electro-Optics*, Vol. 1, LIA, 2014, pp. 834–841.
- [35] J. Smith, W. Xiong, J. Cao, W.K. Liu, Thermodynamically consistent microstructure prediction of additively manufactured materials, *Comput. Mech.* 57 (3) (2016) 359–370.
- [36] T. Keller, G. Lindwall, S. Ghosh, L. Ma, B.M. Lane, F. Zhang, U.R. Kattner, E.A. Lass, J.C. Heigel, Y. Idell, et al., Application of finite element, phase-field, and CALPHAD-based methods to additive manufacturing of Ni-based superalloys, *Acta Mater.* 139 (2017) 244–253.

- [37] Q. Chen, G. Guillemot, C.-A. Gandin, M. Bellet, Three-dimensional finite element thermomechanical modeling of additive manufacturing by selective laser melting for ceramic materials, *Addit. Manuf.* 16 (2017) 124–137.
- [38] D. Zhang, Z. Feng, C. Wang, Z. Liu, D. Dong, Y. Zhou, R. Wu, Modeling of temperature field evolution during multilayered direct laser metal deposition, *J. Therm. Spray Technol.* 26 (5) (2017) 831–845.
- [39] C. Baykasoglu, O. Akyildiz, D. Candemir, Q. Yang, A.C. To, Predicting microstructure evolution during directed energy deposition additive manufacturing of Ti-6Al-4V, *J. Manuf. Sci. Eng.* 140 (5) (2018) 051003.
- [40] J. Li, Q. Wang, P.P. Michaleris, An analytical computation of temperature field evolved in directed energy deposition, *J. Manuf. Sci. Eng.* 140 (10) (2018) 101004.
- [41] D. Rosenthal, The theory of moving sources of heat and its application of metal treatments, *Trans. ASME* 68 (1946) 849–866.
- [42] D. Weisz-Patrault, Fast macroscopic thermal analysis for laser metal deposition. application to multiphase steels, in: *Sim-AM 2019: II International Conference on Simulation for Additive Manufacturing, CIMNE, 2019*, pp. 60–71.
- [43] D. Weisz-Patrault, S. Sakout, A. Ehrlacher, Fast simulation of temperature and grain growth in directed energy deposition additive manufacturing, in: *14th World Congress on Computational Mechanics, Vol. 1, ECCOMAS Congress, 2020*, p. 2748.
- [44] S. Sakout, D. Weisz-Patrault, A. Ehrlacher, Energetic upscaling strategy for grain growth. I: Fast mesoscopic model based on dissipation, *Acta Mater.* 196 (2020) 261–279.
- [45] D. Weisz-Patrault, S. Sakout, A. Ehrlacher, Energetic upscaling strategy for grain growth. II: Probabilistic macroscopic model identified by Bayesian techniques, *Acta Mater.* (2021).
- [46] P. Margerit, D. Weisz-Patrault, K. Ravi-Chandar, A. Constantinescu, Tensile and ductile fracture properties of as-printed 316L stainless steel thin walls obtained by directed energy deposition, *Addit. Manuf.* 37 (2021) 101664.
- [47] Y. Balit, P. Margerit, E. Charkaluk, A. Constantinescu, Crushing of additively manufactured thin-walled metallic lattices: Two-scale strain localization analysis, *Mech. Mater.* 160 (2021) 103915.
- [48] D. Weisz-Patrault, T. Koedinger, Residual stress on the run out table accounting for multiphase transitions and transformation induced plasticity, *Appl. Math. Model.* 60 (2018) 18–33.
- [49] CEA, Cast3m, 2020, Commissariat à l'Énergie Atomique, <http://www-cast3-m.cea.fr/>.
- [50] D. Weisz-Patrault, Multiphase model for transformation induced plasticity. Extended Leblond's model, *J. Mech. Phys. Solids* 106 (2017) 152–175.
- [51] D. Weisz-Patrault, C. Francart, G. Seisson, Uncertainty estimation and hierarchical Bayesian analysis of mechanical dynamic tests, *J. Dynam. Behav. Mater.* 7 (3) (2021) 447–468.
- [52] D. Bäuerle, *Laser Processing and Chemistry*, Springer Science & Business Media, 2013.
- [53] High Temperature Characteristics of Stainless Steels, Technical Report, A Designers' Handbook Series No. 9004. American Iron and Steel Institute, 2011.
- [54] S.S. Lee, U.-S. Min, B. Ahn, S.H. Yoo, Elastic constants determination of thin cold-rolled stainless steels by dynamic elastic modulus measurements, *J. Mater. Sci.* 33 (3) (1998) 687–692.
- [55] Y. Balit, E. Charkaluk, A. Constantinescu, Digital image correlation for microstructural analysis of deformation pattern in additively manufactured 316L thin walls, *Addit. Manuf.* 31 (2020) 100862.